Remote Sensing of Environment 185 (2016) 210–220

Contents lists available at ScienceDirect

Remote Sensing of Environment

journal homepage: www.elsevier.com/locate/rse

Active fire detection using Landsat-8/OLI data

Wilfrid Schroeder [a,*], Patricia Oliva [a], Louis Giglio [a], Brad Quayle [b], Eckehard Lorenz [c], Fabiano Morelli [d]

[a] Department of Geographical Sciences, University of Maryland, College Park, MD, USA
[b] USDA Forest Service Remote Sensing Applications Center, Salt Lake City, UT, USA
[c] Institute of Optical Sensor Systems, German Aerospace Center, Berlin, Germany
[d] Brazilian Institute for Space Research, São José dos Campos, Brazil

ARTICLE INFO

Article history:
Received 6 April 2015
Received in revised form 10 August 2015
Accepted 31 August 2015
Available online 9 September 2015

ABSTRACT

The gradual increase in Landsat-class data availability creates new opportunities for fire science and management applications that require higher-fidelity information about biomass burning, improving upon existing coarser spatial resolution (≥1 km) satellite active fire data sets. Targeting those enhanced capabilities we describe an active fire detection algorithm for use with Landsat-8 Operational Land Imager (OLI) daytime and nighttime data. The approach builds on the fire-sensitive short-wave infrared channel 7 complemented by visible and near-infrared channel 1–6 data (daytime only), while also expanding on the use of multi-temporal analysis to improve pixel classification results. Despite frequent saturation of OLI's fire-affected pixels, which includes radiometric artifacts resulting from folding of digital numbers, our initial assessment based on visual image analysis indicated high algorithm fidelity across a wide range of biomass burning scenarios, gas flares and active volcanoes. Additional field data verification confirmed the sensor's and algorithm's ability to resolve fires of significantly small areas compared to current operational satellite fire products. Commission errors were greatly reduced with the addition of multi-temporal analysis tests applied to co-located pixels, averaging less than 0.2% globally. Because of its overall quality, Landsat-8/OLI active fire data could become part of a network of emerging earth observation systems providing enhanced spatial and temporal coverage of biomass burning at global scales.

1. Introduction

Each year hundreds of thousands of biomass burning related fires are detected globally using spaceborne remote sensing data (Dwyer, Pinnock, Grégoire, & Pereira, 2000; Giglio, Csiszar, & Justice, 2006; Ichoku, Giglio, Wooster, & Remer, 2008). Satellite-detected thermal-anomalies are predominantly associated with land use practices (maintenance and conversion fires), wildfires ignited by lightning or human causes and other natural occurring phenomena or processes (e.g., volcanic activity, etc.). Industrial heat sources can also be detected (Bowman et al., 2009; Schroeder et al., 2008b). Biomass burning effects can be observed across local to global scales, impacting soil chemistry, surface runoff, land surface heat and energy balances, and air quality, among others (Larsen et al., 2009; Liu, Randerson, Lindfors, & Chapin, 2005; Wiedinmyer et al., 2006). Negative ecological effects may result from biomass burning in non-fire-adapted vegetation or as a consequence of altered fire regimes (e.g., encroachment of invasive species and changes to stand structure), whereas positive effects are typically observed in fire-adapted biomes that benefit from nutrient cycling and seeding (Freeman et al., 2007; Higgins et al., 2007; Oliveras et al., 2012). In areas such as the western United States, southern Australia, and the Iberian Peninsula, large wildfires occurring along the wildland-urban interface pose risks to both life and property and are cause of major socioeconomic concern (Mell, Manzello, Maranghides, Butry, & Rehm, 2010). Management efforts associated with those events typically involve large investments in fuel treatments, community response planning, active fire mapping and suppression, and post-fire stabilization and restoration (Schoennagel, Nelson, Theobald, Carnwath, & Chapman, 2009).

For more than a decade, satellite remote-sensing active fire data have been extensively used to inform fire management systems (Davies, Ilavajhala, Wong, & Justice, 2009). Similarly, numerous air-quality and carbon emissions mapping methodologies have benefited from point source information provided by satellite active fire detection and characterization data sets (Ichoku & Kaufman, 2005; Kaiser et al., 2012; van der Werf et al., 2010; Vermote et al., 2009). Other related active fire data applications include assessment of fire-affected areas and seeding of burned area algorithms (Giglio, Loboda, Roy, Quayle, & Justice, 2009; Hantson, Padilla, Corti, & Chuvieco, 2013; Loboda, O'Neal & Csizar 2007; Kasischke, Hewson, Stocks, van der Werf, & Randerson, 2003; Oliva & Schroeder, 2015), fire growth and spread rate analyses

* Corresponding author at: Department of Geographical Sciences, University of Maryland, 2181 LeFrak Hall, College Park, MD 20742, USA.
E-mail address: wschroed@umd.edu (W. Schroeder).

http://dx.doi.org/10.1016/j.rse.2015.08.032

(Csiszar & Schroeder, 2008; Loboda & Csizar, 2007; Pozo, Olmo, & Alados-Arboledas, 1997), and detection of fossil fuel emissions sources from gas flares (Casadio, Arino, & Serpe, 2012; Elvidge et al., 2009; Elvidge, Zhizhin, Hsu, & Baugh, 2013), among others.

The use of Landsat-class data to detect thermal anomalies has been successfully demonstrated in previous studies. For example, Francis and Rothery (1987) and Oppenheimer (1991) applied near infrared (NIR) and short-wave infrared (SWIR) Landsat-5 Thematic Mapper data to case study analyses of volcanic activity. Others expanded on thermal anomalies applications to include long-wave infrared data from Landsat-5 Thematic Mapper (TM) and Landsat-7 Enhanced Thematic Mapper Plus (ETM+) (Flynn, Harris, & Wright, 2001; Anejionu, Blackburn, & Whyatt, 2014). A more generic application of NIR and SWIR Landsat-class data to detect actively burning fires was also demonstrated (Giglio et al., 2008; Schroeder et al., 2008a). However, because of limited data availability and access restrictions previous studies using those active fire data were mainly focused on regional validation analyses of active fire products derived from the 1-km Moderate Resolution Imaging Spectroradiometer (MODIS) and the 4-km Geostationary Operational Environmental Satellite (GOES) imager (Csiszar, Morisette, & Giglio, 2006; Morisette, Giglio, Csiszar, & Justice, 2005; Schroeder et al., 2008a).

While the spatial and temporal coverage provided by individual Landsat-class sensors remained relatively unchanged over the years, the adoption of free data policies and the launch of new instruments by international agencies helped gradually increase the availability of Landsat-class data creating renewed opportunities for biomass burning applications. The current United States Geological Survey (USGS) Landsat, China-Brazil Earth Resources Satellite (CBERS), Indian Resourcesat, and European Space Agency Sentinel-2 programs are good examples of the growing number of Landsat-class assets serving the broader user community. Compared to traditional ≈1-km spatial resolution satellite fire products, Landsat-class data offer significantly improved mapping capability generating detailed fire line information. Those assets have the potential to transform the way satellite data are used in support of fire management, adding to current airborne tactical fire mapping resources, for example, and providing consistent and reliable fire information to decision support systems operating at similar spatial scales. A direct application of such concept was demonstrated by Coen and Schroeder (2013, 2015), who successfully used spatially refined satellite fire data to initialize and later verify coupled weather-fire model simulations of large long-duration wildfires in the western United States.

In this study, we present an active fire detection algorithm for use with the Landsat-8 day and nighttime data. The approach builds on previous algorithms applied to the Advanced Spaceborne Thermal Emission and Reflection Radiometer (ASTER) and Landsat-7 ETM+ NIR and SWIR data while further expanding the use of multi-temporal analysis to improve the classification of individual pixels.

2. Input Data

Landsat-8 was designed by the National Aeronautics and Space Administration (NASA) and launched on 11 February 2013 carrying the Operational Land Imager (OLI) and the Thermal Infrared Sensor (TIRS), and subsequently transferred to USGS for routine operations (Roy et al., 2014). Placed on a sun-synchronous orbit at 705 km altitude and 10:00 a.m. equatorial crossing time for the descending node, Landsat-8 has a 16-day repeat cycle although data acquisition strategy may vary based on geographic coverage (including seasonal sampling and cloud coverage) and overall science mission objectives (Irons, Dwyer, & Barsi, 2012; Roy et al., 2014). In this study, we used standard terrain corrected (Level 1 T) data from OLI, which is a nine spectral channel push-broom sensor with a spatial resolution of 30 m (15 m for the panchromatic channel 8), and an individual scene size of 185 km × 180 km matching the second World-wide Reference System (WRS-2) of path and row coordinates (Irons et al., 2012). Quantized and calibrated scaled digital numbers (DNs) for each OLI band are delivered as 16-bit unsigned integers. Those are converted to top-of-atmosphere (TOA) spectral radiance and planetary reflectance values using the rescaling coefficients found in the metadata (MTL) file available with the L1T data.

The Landsat-8 active fire detection builds on previous algorithms developed for ASTER and Landsat-7 ETM+ (Giglio et al., 2008; Schroeder et al., 2008a). Both methodologies used a two-channel fixed-threshold plus contextual approach exploring the differential radiometric response of the SWIR (channel 8 on ASTER; channel 7 on ETM+) and the NIR (channel 3 N on ASTER; channel 4 on ETM+) data to classify fire-affected pixels. Here, we expand on that original methodology using top-of-atmosphere spectral reflectance data from seven different OLI channels. The list of OLI channels used by the fire algorithm is shown on Table 1, along with their intended application. Complementing the input OLI data described on Table 1, pixel-based cloud coverage information is derived from the auxiliary quality band (cloud confidence bits 14–15) for use in the multi-temporal analysis discussed in Section 4.

As with ASTER and ETM+ data, active-fire-affected pixels may often exceed the maximum resolvable radiance on OLI's fire-sensitive SWIR channel 7, causing frequent pixel saturation. Spurious DN values and artificial radiances may be output by the analog-to-digital converter when the input signal exceeds the nominal detector range. Under more extreme conditions when large and/or very high temperature fires occupy the pixel footprint the increased radiance input to the detector can also lead to folding of the pixel's DN (also known as oversaturation (Morfitt et al., 2015)). This less frequent anomaly is typically characterized by pixels of abnormally low OLI channel 7 radiance values located near the core of actively burning fire perimeters, an artifact resulting from the DN folding, accompanied by elevated radiance on the shorter wavelength channels 6 and 5. Fig. 1 shows a manifestation of the DN folding on channel 7 coinciding with the large and energetic Rim fire complex in California/U.S., imaged on 31 August 2013. A small subset of the fire perimeter on channel 6 reveals a 15 pixel wide area of elevated radiances near the core, whereas the co-located channel 7 data show a ring of elevated radiances around an anomalous low-radiance core indicative of DN folding. The graphs on Fig. 1 show the channel 6 and 7 radiance profiles drawn across the active fire, and the histogram for channel 7 radiances coincident with a larger sample consisting of over 4500 fire-affected pixels on the scene. The channel 6 profile shows high radiance values near the center of the fire, including pixels at or above the nominal saturation of 71.3 W/(m^2 sr μm). The same core area shows near-zero and artificially low channel 7 radiance values surrounded by other pixels at or above the nominal saturation of 24.3 W/(m^2 sr μm), therefore describing a typical DN folding scenario. We note that the maximum observable radiance on channels 6 and 7 are 96 and 29 W/(m^2 sr μm), respectively (Morfitt et al., 2015).

The histogram in Fig. 1 shows the highest number of pixels associated with the Rim fire with radiance values around the nominal saturation on channel 7. In addition, a non-negligible number of pixels with radiance values above the nominal saturation are found as a result of analog high saturation. A few pixels corresponding to DN folding are found

Table 1
List of 30 m resolution Landsat-8/OLI channels used in the active fire detection algorithm, and their primary application.

OLI channel	Wavelength (μm)	Application
1	0.43–0.45	Active fire detection & water mask
2	0.45–0.51	Water mask
3	0.53–0.59	Water mask
4	0.64–0.67	Water mask
5	0.85–0.88	Active fire detection & water mask
6	1.57–1.65	Active fire detection & water mask
7	2.11–2.29	Active fire detection, water mask & temporal analysis

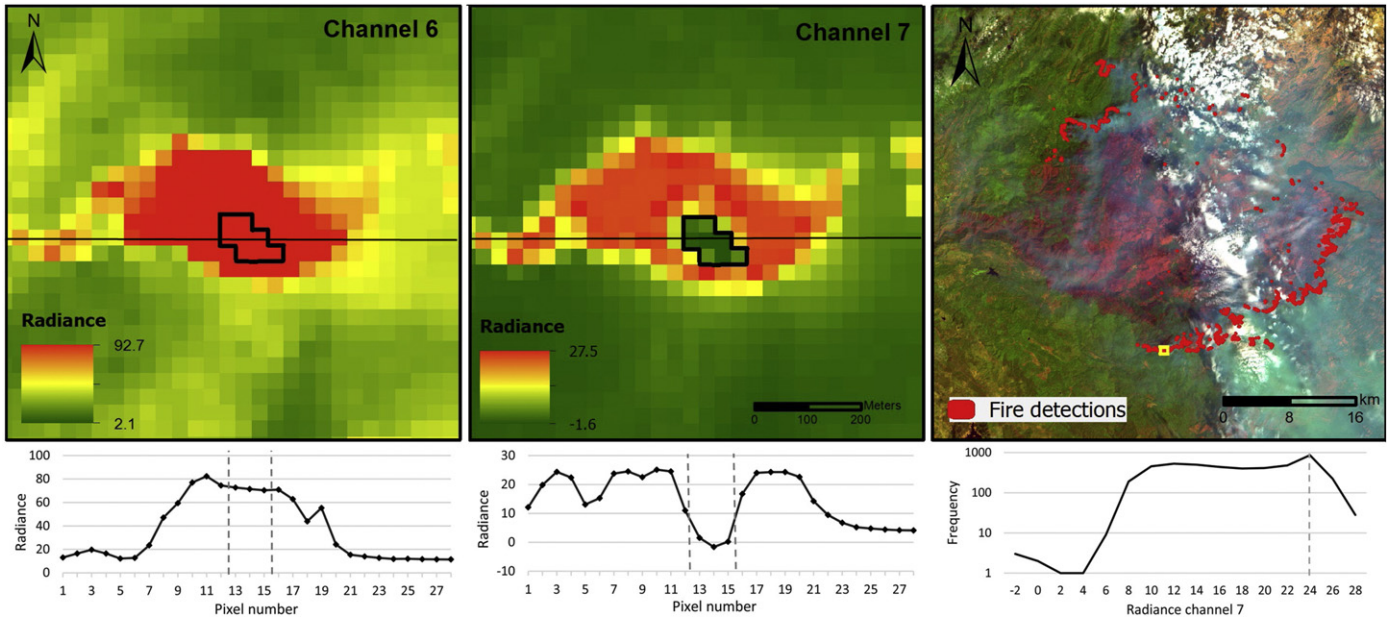

Fig. 1. Landsat-8/OLI channel 6 (top-left) and 7 (top-center) image subsets acquired on 31 August 2013 over the Rim fire in California/U.S (37.760°N 119. 965°W; path/row 43/34). The low radiance fire core on channel 7 is indicative of DN folding. The radiance profiles (bottom-left, bottom-right) correspond to the horizontal line across each subset. The spurious drop in channel 7 radiance is the result of DN folding; the same pixels show saturated radiances on channel 6. The histogram describing channel 7 radiances for all 4500 fire-affected pixels (marked in red) in the top-right image subset is shown on the bottom-right panel. The peak in the radiance distribution coincides with the nominal saturation radiance (24.3 W/(m^{2}srμm)). Pixels exceeding the nominal saturation are representative of analog high saturation. A small number of pixels describing DN folding can be found near the low end of the radiance range. The small yellow box in the top-right panel indicates the area subject to DN folding.

near the low end of the radiance range on channel 7. While this particular case describes characteristics associated with significant fire intensity for a major wildfire event, folding of OLI channel 7 DN can also be observed over some large gas flares.

3. Active fire algorithm

The Landsat-8 active fire detection algorithm is divided into day and nighttime modules. Both detection modules are driven by the fire-sensitive SWIR channel 7 data, exploiting the emissive component of fires in the 2.2 μm spectral window. During the daytime orbits the emissive fire component is mixed with the background, which is dominated by the reflected solar component. In order to separate those, we use the NIR channel 5 data that are mostly unresponsive to fire-affected pixels, though highly correlated to the SWIR channel data over fire-free surfaces (Giglio et al., 2008). During night orbits the reflected solar component is absent from the scene, making the SWIR band particularly responsive to the emitted radiance from active fires in an otherwise dull background. In both day and nighttime data, the radiometric signature of active fires produces a SWIR radiance or reflectance anomaly

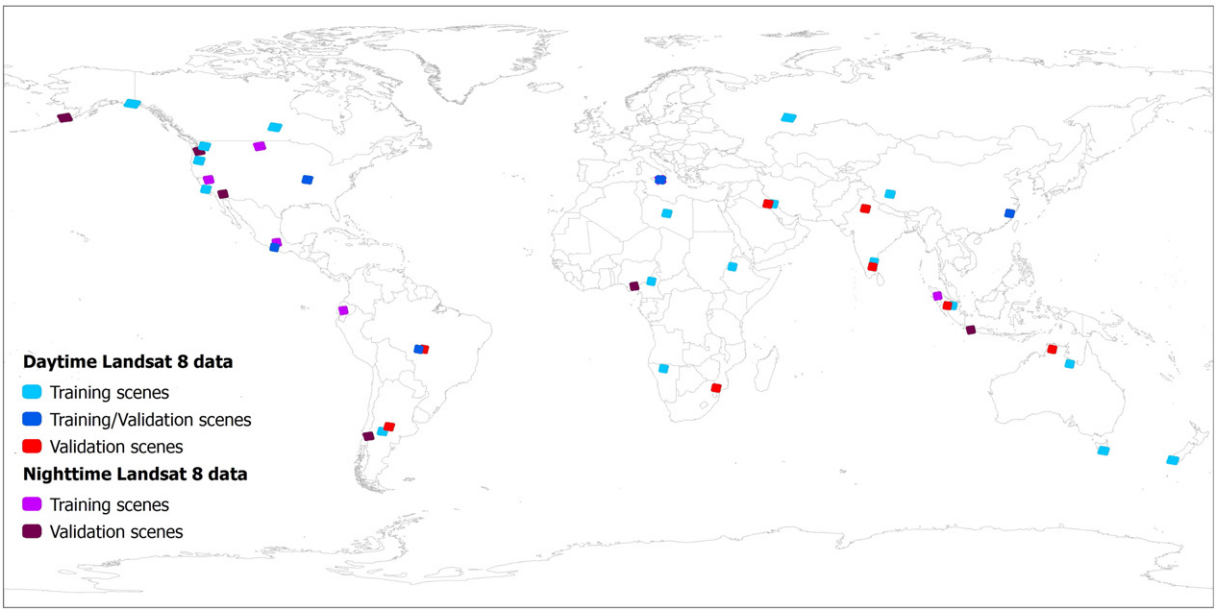

Fig. 2. Geographic distribution of primary Landsat-8/OLI Level 1 T scenes used for training and validation of the active fire detection algorithm.

when compared to the background, thereby mimicking the concept of thermal anomaly detection using mid-to-thermal infrared channels.

Fig. 2 shows the distribution of Landsat-8 scenes used to train and later validate the fire algorithm output. Scene selection allowed sampling of a wide range of fire and observation conditions. Co-located scenes indicate areas where multi-temporal data acquisitions were obtained, with training and validation data analyzed separately. The training data were used to calibrate the algorithm and were based primarily on histogram analysis of single channel and dual-channel (e.g., band ratios and differencing) data supported by detailed supervised pixel classification information. The latter was performed by expert image analysts and corroborated by high spatial resolution imagery (e.g., aerial photography and commercial satellite imagery available in Google Earth) and other remotely sensed fire products. These supporting data were used to validate fire activity identified by the detection algorithm. The algorithm thresholds were defined for TOA reflectance data that have not been corrected for solar elevation.

3.1. Daytime detection

The daytime algorithm uses input data from all seven OLI channels listed in Table 1. The first test in the daytime module is designed to identify potentially unambiguous active fire pixels. It builds on the ETM+ active fire algorithm (Schroeder et al., 2008a) while accommodating small differences in OLI spectral channels, and is based on the following condition:

$$\{R_{75}>2.5 \text{ AND } \rho_7-\rho_5>0.3 \text{ AND } \rho_7>0.5\} \quad (1)$$

where ρ_i is the reflectance on channel i, and R_{ij} is the ratio between channel i and j reflectances (*i.e.*,ρ_i/ρ_j).

As described in Section 2, highly energetic and extensive fires can lead to folding of the DN on channel 7 thereby characterizing another condition of potentially unambiguous active fire pixel. Those unique occurrences are flagged using:

$$\{\rho_6>0.8 \text{ AND } \rho_1<0.2 \text{ AND } (\rho_5>0.4 \text{ OR } \rho_7<0.1)\}. \quad (2)$$

Complementing the identification of unambiguous fire pixels, the thresholds in test (1) are relaxed and other candidate fire pixels are selected for further analyses based on the following criteria:

$$\{R_{75}>1.8 \text{ AND } \rho_7-\rho_5>0.17\}. \quad (3)$$

All pixels satisfying test (3) must then meet the following set of fixed threshold and contextual tests in order to be classified as potential fire-affected pixels:

$$R_{75}>\overline{R_{75}} + max\left[3\sigma_{R_{75}}, 0.8\right] \quad (4)$$

AND

$$\rho_7>\overline{\rho_7} + max\left[3\sigma_{\rho_7}, 0.08\right] \quad (5)$$

AND

$$R_{76}>1.6 \quad (6)$$

where $\overline{R_{ij}}$ and $\sigma_{R_{ij}}$ ($\overline{\rho_7}$ and σ_{ρ_7}) are the mean and standard deviation calculated for the band ratio (channel 7 reflectance) using valid background pixels from a 61 × 61 window centered on the candidate pixel. Valid pixels are defined as those showing channel 7 reflectance greater than zero, excluding water and unambiguous fire pixels. Water pixels are classified based on spectral profiling using reflectance data from all seven input channels. Two distinct tests are applied in order to map oceans and inland water bodies according to:

$$\{\rho_4>\rho_5 \text{ AND } \rho_5>\rho_6 \text{ AND } \rho_6>\rho_7 \text{ AND } \rho_1-\rho_7<0.2\} \quad (7)$$

AND

$$\{(\rho_3>\rho_2) \quad (8)$$

OR

$$(\rho_1>\rho_2 \text{ AND } \rho_2>\rho_3 \text{ AND } \rho_3>\rho_4)\}. \quad (9)$$

Tests (7 & 8) capture shallow and/or sediment-rich waters (e.g., Amazon river mouth) whereas tests (7 & 9) are useful for mapping deep and/or dark water bodies. This water-masking scheme resulted in a more liberal classification compared to the available water confidence bits in the L1T quality band, allowing more water pixels to be flagged albeit with some errors of commission. For example, tests (7 & 9) may confuse water bodies and cloud shadows and thereby affect the valid background statistics, although such classification errors had no noticeable effect on the fire algorithm performance.

3.2. Nighttime detection

The absence of the reflected solar component from the nighttime scenes makes the classification of fire-affected pixels significantly less challenging. Here we use a single fixed-threshold test based on the SWIR channel 7 radiance data and similar to Giglio et al. (2008):

$$L_7>1 \text{ W}/(\text{m}^2 \cdot \text{sr} \cdot \mu\text{m}) \quad (10)$$

Where L_7 is the channel 7 radiance. We did not encounter evidence of DN folding in the nighttime scenes analyzed. We recognize, however, that our assessment was limited by the reduced availability of nighttime scene acquisitions. Additional tests using channel 6 radiance data may be required to properly handle DN folding in those data.

4. Multi-temporal analysis

The Level 1T OLI data have a geolocation error requirement of 12 m (Irons et al., 2012), greatly improving the co-location of surface features observed on images acquired over multiple dates. Building on the enhanced geolocation data, we designed a simple procedure to help refine the fire algorithm output using co-located data derived from previous images acquired no more than 176 days apart. This temporal constrain was applied in order to minimize the effects of seasonal variations that could potentially alter the land surface conditions, while balancing cloud-free data availability.

The approach is based on direct verification of previously processed active fire data for spatially-coincident and temporally-persistent fire pixels. This simple test is based on the assumption that typical biomass burning fuels within a 30 m ground footprint are completely consumed within minutes, hours, or a few days of continuous flaming and/or smoldering combustion. Therefore pixels classified as potential fire-affected areas by the detection algorithm that overlap with one or more previously detected fire pixels are assigned a *persistent source* class indicative of temporally persisting detection. Such classification was found useful to flag gas flares and other stationary urban heat sources (e.g., steel mills). Consequently, it can be used to differentiate between open vegetation fires and other types of combustion or heat sources. Additionally, this test may flag potential daytime commission errors (false alarms) associated with radiometrically bright urban features (e.g., hot and reflective factory rooftops) and other unique structures such as solar farms/photovoltaic stations, etc. We note that charcoal pits and repeated piling of biomass for burning in designated areas may also be flagged as persistent sources as a result of this test.

Pixels output by the daytime fire algorithm without a co-located detection in the previous 176 days are further inspected to check for the occurrence of high channel 7 reflectances persisting over time, an indication of potential false alarm. We used channel 7 for this test due to its strengths in separating vegetated and non-vegetated (e.g., bare soil) surfaces, and reduced contamination by smoke (Asner & Lobell, 2000; Kaufman et al., 1997). The test assigns a *bright surface* class to those pixels with $\rho_{7,t} > 0.2$, which describes the mean channel 7 reflectance calculated using t co-located cloud-free pixels in the previous 176 days. This additional test is designed to flag pixels in areas dominated by urban environment or exposed soils that, under specific illumination conditions, can mimic the biomass-burning signature causing a false alarm. Those targets may also be found in association with pixels adjacent to persistent urban detections, where the increased distance to the heat/high reflectivity source results in less frequent manifestation of reflectance anomalies.

The application of the multi-temporal analysis component is demonstrated in Fig. 3, which shows an OLI image subset over eastern China (path/row 119/41). Potential false alarms associated with radiometrically bright urban structures can be seen on the fire algorithm output. Detailed visual inspection of those locations revealed factories and other facilities consisting of large reflective rooftops and heat exhausts. Application of the complementary multi-temporal analysis tests to those pixels resulted in successful re-classification of all pixel locations, setting them apart from actual biomass burning activity in neighboring rural areas.

5. Theoretical fire detection envelope

Satellite fire data users are fundamentally interested in the resolving power of new algorithms, in other words, what minimum fire size can be typically detected? Effective quantification of satellite fire detection performance using ground truth data can be challenging due to lack of adequate reference data and, most importantly, because of the high costs involved. Alternatively, theoretical calculation of detection curves as a function of fire size and temperature provides useful information to assess individual algorithms, and to compare between different fire products.

Here we calculated the fire algorithm's day and nighttime detection curves separately. The daytime fire detection curve calculation built on the approach of Schroeder, Oliva, Giglio, and Csiszar (2014), who assessed the performance of the Suomi National Polar-orbiting Partnership Visible Infrared Imaging Radiometer Suite (S-NPP/VIIRS) 375-m active fire detection algorithm using actual data. We selected 12 different OLI images acquired globally, each representing a distinct geographic area at times coinciding with their respective active fire seasons. Fire activity varied among individual scenes, ranging from as few as 79 pixels (Northern Territory/Australia) to a maximum of 6561 pixels (Central Siberian Plateau/Russia). For each scene, a total of 25 pixels were selected across the entire domain. Pixel selection included areas adjacent to active fires (simulating an extended fire line), clouds and water bodies, subject to smoke plumes, and across a wide range of vegetated and non-vegetated areas (randomly sampled). Fires were then simulated on those individual pixels by incorporating fire-emitted radiance to OLI's primary channels 5, 6, and 7. Simulated pixel radiances were converted back to scaled DN, and then to reflectance using the corresponding MTL file parameters. Atmospheric attenuation effects were estimated using a radiative transfer code (MODTRAN®) running on atmospheric profiles derived from the National Oceanic and Atmospheric Administration (NOAA) Global Forecast System (GFS) model analysis data for each scene selected. Fire effective areas were varied between 1 and 150 m^2 (1 m^2 intervals), and mean temperatures were varied between 400 and 1200 K (10 K intervals). Simulated single-component fire radiances were calculated with consideration to the fractional area coverage and the spectral response function of each channel, and then added to the selected pixel radiances. In order to ensure optimum representation of observable conditions, all background pixels were preserved resulting in realistic fire-affected synthetic images. These synthetic data were processed using the daytime fire algorithm without any modification. Fig. 4 shows the 50% probability of fire detection curve derived from all 3.6 million data points resulting from the simulation scenarios above. The curve shows a noticeable increase in fire detection performance compared to other coarser spatial resolution fire data

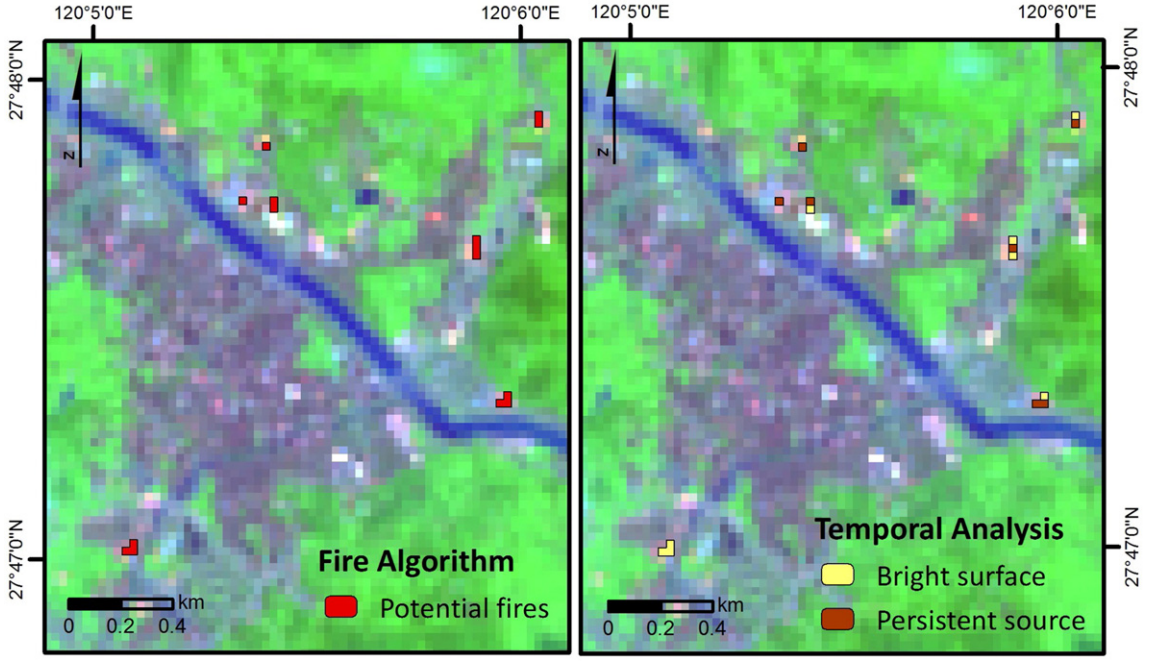

Fig. 3. Subset of 07 August 2014 Landsat-8/OLI image of eastern China (path/row 119/41). Green shades indicate vegetation, gray and magenta shades indicate urban areas. Left panel shows pixels output by the fire algorithm; right panel shows the corresponding multi-temporal analysis result with all pixels re-classified as urban-related heat/highly reflective sources.

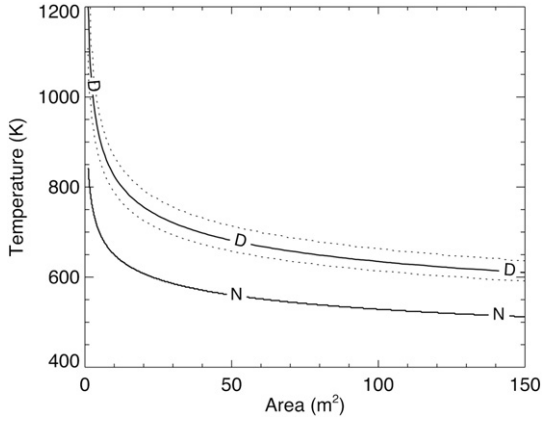

Fig. 4. Theoretical probability of fire detection calculated for the Landsat-8 algorithm. Daytime (D) curve describes the 50% probability of detection (solid line), bounded by 10% (bottom dotted line) and 90% (top dotted line) probability curves. The nighttime (N) curve describes the fire area and temperature combination resulting in OLI channel 7 radiance greater than 1 W/(m^2srμm).

products (e.g., S-NPP/VIIRS) (Schroeder et al., 2014), with typical firewood combustion (950 K mean temperature) requiring ≈ 4 m^2 of effective fire area to achieve greater than 50% chance of detection.

Our assessment of the nighttime probability of detection curve was based on a simplistic approach involving direct calculation of fire-emitted radiances from the same set of fire effective area and mean temperatures described above. We assumed a near-zero and invariant nighttime background radiance, which leaves the simulated fire-emitted radiance as the only potential source influencing the resulting pixel radiance. Similar to the daytime simulations, atmospheric attenuation effects were estimated using MODTRAN® assuming a U.S. standard atmospheric profile. Fig. 4 shows the night curve describing the fire area and temperature combination leading to a channel 7 radiance of 1 W/(m^2 sr μm), which would potentially allow for the fire pixel detection. Compared to the daytime curve, nighttime data provide enhanced response to smaller fires of similar temperature favored by the exclusion of the reflected solar component. For example, the same typical firewood combustion burning at ≈950 K may be detected when effective fire areas as small as 1 m^2 are observed.

The data simulations above did not account for the occurrence of optically thin or thick clouds and smoke, or the pixel's spatial response function. Therefore they describe a best-case scenario of fire detection, which may be subject to partial or complete degradation depending on the prevailing observation conditions.

6. Algorithm Assessment

Initial algorithm assessment was based on visual inspection of the output fire pixel coordinates using publicly available data including high spatial resolution imagery (e.g., aerial photography, high resolution commercial satellite imagery in Google Earth). The fidelity of the fire detection data was qualitatively assessed by expert image analysts over a wide range of fire conditions, including large/unambiguous and well-documented biomass burning (e.g., boreal fires in Canada, wildfires in western U.S.), variable size land management fires (e.g., grassland fires in Africa, conversion fires in the Amazon, agricultural fires in India), small point sources associated with known gas flare locations (e.g., gas fracking stations in North Dakota/U.S., and oil fields in the middle-east), and other verifiable thermal anomalies such as active volcanoes.

The Landsat-8 fire algorithm performed well across the wide range of conditions described above. Fig. 5 shows the daytime fire detections produced for the 2014 King fire in California/U.S., corroborated by same-day fire detections derived from 1-km Terra and Aqua MODIS Thermal Anomalies (MOD14/MYD14), and 750 m and 375-m S-NPP/VIIRS active fire data (Csiszar et al., 2014; Giglio, Descloitres, Justice, & Kaufman, 2003; Schroeder et al., 2014). Those satellite images were acquired sequentially, averaging 1-h separation between consecutive overpasses. Overall, the different products showed good correspondence both in terms of fire front location and extent. Notably though, Landsat-8 fire pixels provided a significantly more detailed mapping of the flaming front describing areas of continuous activity on both east and west flanks of the fire, plus isolated heat islands inside the perimeter. The formation of an optically thick pyrocumulus cloud at the northern section (leading edge) of the fire perimeter had variable effects on the fire products as it evolved throughout the day. Other areas dominated by relatively dry smoke showed no noticeable effect on the OLI SWIR reflectances and the corresponding fire detection performance (Supplementary material).

Quantitative daytime commission error rates of the algorithm were estimated for 13 different locations showing very distinct levels of fire activity (Table 2). Processing of individual scenes included the main fire algorithm and the complementary multi-temporal analysis procedure described above. The number of usable scenes included in the temporal analysis was dependent on cloud coverage. Argentina and north India were particularly affected by cloud obscuration, with less than five of the eleven possible scenes acquired in the previous 176 days showing cloud-free data. Despite the smaller number of scenes used in the multi-temporal analysis the algorithm was able to correctly classify active fires, persistent thermal sources, and bright pixels with zero or negligible commission error rate.

Six regions of markedly different fire characteristics showed a large number (> 1000) of pixels detected, namely South Africa, Australia, Brazil, Mexico, north India and Iraq. In South Africa and Australia, detected pixels described large wildfires on each scene. Forest conversion and pasture maintenance fires were found in Brazil, whereas agricultural fires dominated the scenes in Mexico and north India. The scene in Iraq overlapped with oil fields containing numerous gas flare stations.

Application of the multi-temporal analysis tests to the locations above showing high land use related biomass burning activity and wildfires resulted in almost no change in pixel classification. The relatively few cases of pixel re-classification were associated with surface coal mines (Africa), and with urban structures and scarce vegetation pixels in other areas. In comparison, application of the multi-temporal analysis tests to the scene in Iraq produced significant changes resulting in successful re-assignment of all gas flare pixels to the *persistent source* class. Commission errors were negligible in all six regions.

The scene in China coincided with urbanized areas characterized by large factories with highly reflective rooftops. The fire algorithm output indicated 179 pixels of potential fire activity. Of those, 153 were re-classified by the temporal analysis tests into either *persistent source* (50%) or *bright surface* (50%). Of the remaining pixels (26), nine were also coincident with other factories and urban structures indicative of potential false alarms resulting in the highest relative false alarm rate of 34.6%. Indonesia was the region showing the second highest commission error rate. In that case, 65 pixels were output by the fire algorithm and only three were subsequently re-classified by the temporal analysis tests. Of the 62 remaining pixels, 10 pixels were co-located with an industrial park and therefore considered potential false alarms. Pixels associated with potential false alarms consisted predominantly of single detections (52%) and small clusters of two adjacent detections (32%). The largest single cluster associated with potential false alarm showed six contiguous pixels overlapping a large industrial complex in Indonesia. Overall, global daytime commission error rate was equivalent to 0.2%.

Complementing the daytime fire algorithm assessment, Fig. 6 shows the fire detections produced for the nighttime OLI image (path/row 127/217 ascending node) acquired on 04 February 2014 over part of North Dakota/U.S. Numerous gas fracking sites are evident in the high resolution image of that area, all characterized by small land clearings. By zooming into individual sites, we could co-locate all fire pixel

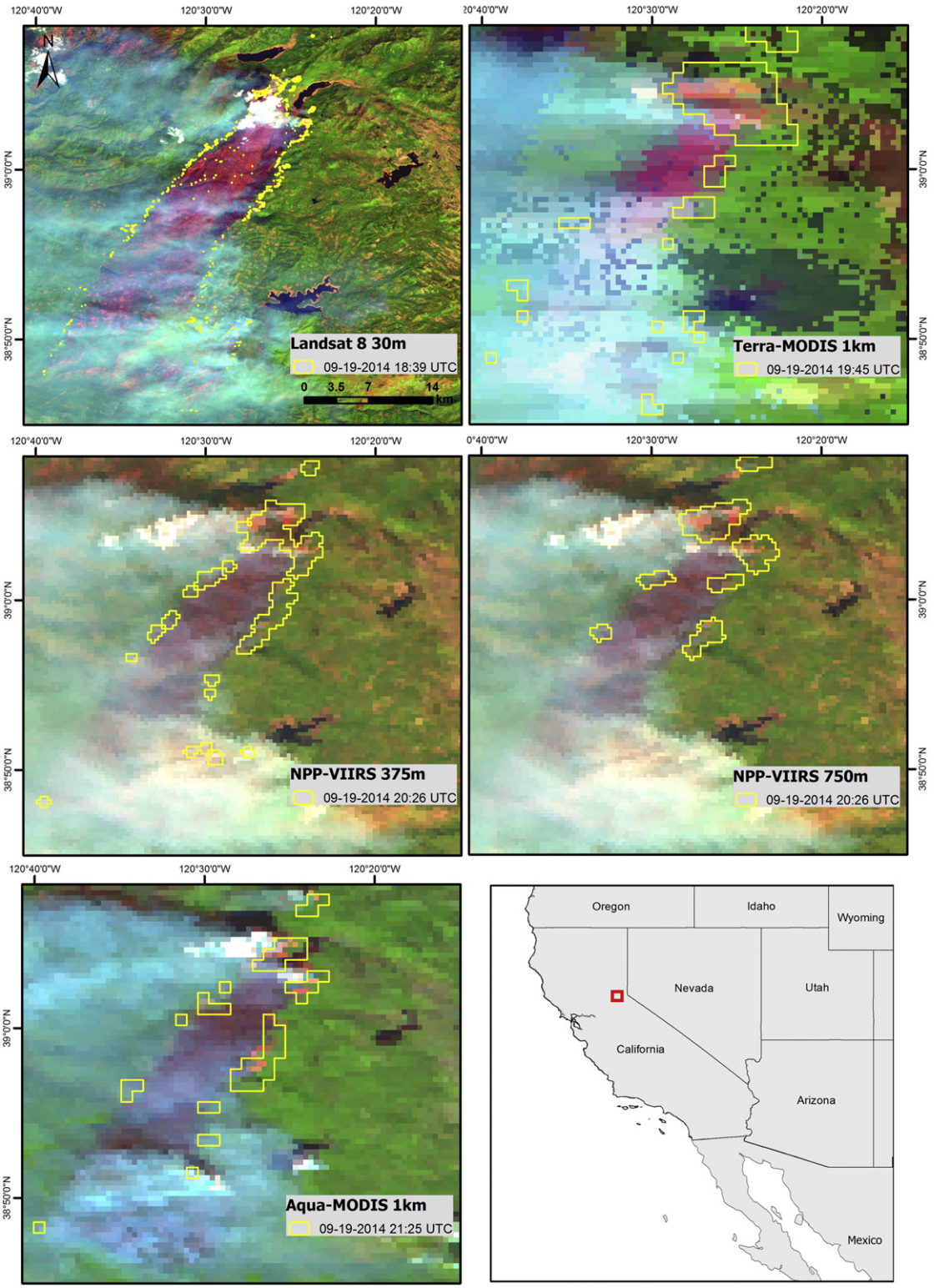

Fig. 5. Multi-sensor imaging of the King fire in California/U.S. on 19 September 2014. Active fire detections derived from Terra/MODIS 1 km, Landsat-8/OLI 30 m (path/row 43/33), S-NPP/VIIRS 375 m and 750 m, and Aqua/MODIS 1 km are marked in yellow. Temporal separation between consecutive images was limited to approximately 1 h.

detections with discernable gas flare stacks on the reference imagery. With the exception of one undetected location with a channel 7 radiance of 0.55 W/(m^2 sr μm), other fracking sites in the image subset showed no discernible heat signatures from the background. We assumed the gas flares in those areas could be temporarily out of service or else burning at a much reduced combustion rate relative to their neighbors, therefore falling below the sensor's minimum resolvable radiance range. This and other regions inspected showed no evidence of false alarms. As a result, we concluded that nighttime commission errors were negligible. Because of the limited number of nighttime scenes available, we could not assess the effect of the multi-temporal analysis tests in those cases.

Table 2
Description of Landsat-8 fire algorithm validation results according to scene location and acquisition date, number of previously acquired scenes used in the multi-temporal analysis, number of pixels output by fire algorithm, number of pixels re-classified as a result of multi-temporal analysis, and estimated commission error rates. The latter describe the percentage of fire algorithm output pixels that were found to be associated with urban pixels (e.g., factories), after exclusion of pixels re-classified by the multi-temporal analysis.

Region	Path/row	Date (dd/mm/yy)	Number of usable scenes	Fire algorithm output pixels	Pixels re-classified (temporal analysis)	Commission Error (%)
Italy	188/034	23/06/14	10	176	3	1.2
Brazil	227/069	24/06/14	9	355	2	0.0
Brazil	226/069	20/08/14	6	1715	1	0.0
Mexico	026/048	07/05/14	9	1345	6	0.0
USA	023/034	18/05/14	7	27	3	4.8
Australia	105/069	05/08/14	8	3533	0	0.0
Indonesia	127/060	14/06/14	8	65	3	16.1
India (north)	147/040	07/05/14	4	4737	73	0.1
India (south)	143/052	24/03/14	6	444	23	1.7
Argentina	229/085	13/01/14	3	184	1	0.0
Iraq	166/039	19/10/14	9	1400	1289	0.0
South Africa	168/077	15/09/14	10	7154	3	0.0
China	119/041	07/08/14	8	179	153	34.6

6.1. Field verification

Data from two field experiments were also used in support of the fire algorithm assessment. On both occasions, a small plot consisting mostly of firewood arranged in a rectangular fuel bed was set up in a rural area and sampled using ground instrumentation. The first experiment (*Exp1*) was coordinated by the German Aerospace Center (DLR) and implemented on 17 August 2013 near Demmin/Germany. The burn plot measured 11 × 13 m^2 and was actively burning during the Landsat-8 overpass (path/row 194/22) at 10:10 UTC. The approximate mean fire temperature estimated using a handheld Heitronics thermal sensor was equivalent to 970 K. The second experiment (*Exp2*) was coordinated by the Brazilian Institute for Space Research (INPE) and implemented on 19 January 2015 near Cachoeira Paulista/Brazil. A smaller burn plot measuring 3 × 10 m^2 was sampled using two uncooled thermal infrared FLIR cameras mounted on tripods positioned adjacent to the fire, plus a dual-band radiometer attached to a 5 m tower at a 45° viewing angle. At the time of the Landsat-8 overpass (path/row 218/076) at 12:58 UTC the fire was actively burning with a temperature of 870 ± 153 K.

Based on the fire characteristics describing the experimental plots above and the theoretical detection envelope calculated for the Landsat-8 fire algorithm in Section 5, both sites had high probability of detection. Processing of the two scenes using the fire algorithm and the temporal analysis tests resulted in two confirmed fire detection pixels overlapping each of the experimental plots. Fig. 7 shows the two experimental plots and the corresponding channel 7 radiance data subset, plus the resulting fire algorithm output with detection pixels marked in black. The maximum observed radiance on channel 7 was equivalent to 27.33 and 24.66 W/(m^2 sr μm) in *Exp1* and *Exp2*, respectively. Consequently, both fires exceeded the nominal channel 7 saturation value. In comparison, the adjacent fire-free pixels showed a mean radiance of 2.32 and 3.23 W/(m^2 sr μm) for *Exp1* and *Exp2*, respectively.

Additional pixels of elevated radiance on channel 7 bordered the two detections on each scene. We attributed those above-background radiance values to smearing caused by the geometric transformations used to convert the OLI Level 1R image (a 2D space consisting of image sample/line) to the Level 1 T data (an implicit 3D space consisting of x/y/z projection coordinates), which accounts for the detectors' spatial response, observation geometry (line-of-sight), terrain (digital elevation model), and pixel spatial interpolation method (cubic convolution) used to produce the output resampled data in Universal Transverse Mercator (UTM) projection (U.S. Department of the Interior – U.S. Geological Survey, 2013). Stray light effects may also contribute to the observed smearing (Morfitt et al., 2015). Such data artifact was systematically observed over fires corresponding to small/point sources such as gas flares occurring in both day and nighttime images. Nonetheless we expect smearing to equally affect larger fires. In fact, visual inspection of training and validation data frequently showed pixels of intermediate (above-background) radiance values adjacent to pixels classified as fires. Those locations were classified as fire-free pixels by our detection methodology and not considered omission errors. Additional validation analyses using high resolution (≈1 m) reference fire data are needed to further corroborate the current results.

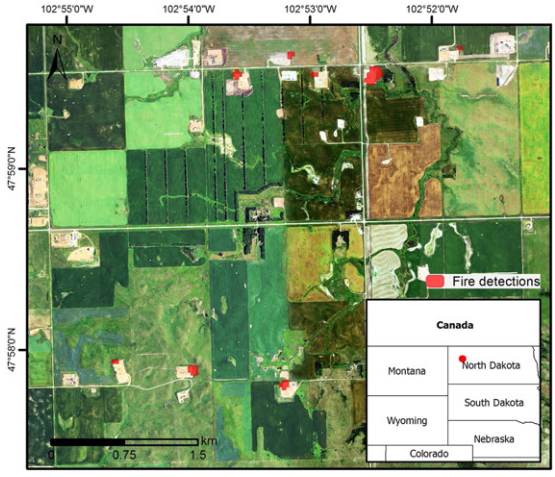

Fig. 6. Subset of the fire detection algorithm output (red polygons) derived from the 04 February 2014 Landsat-8/OLI nighttime scene path/row 127/217 (ascending node) over part of North Dakota/U.S. Background image shows 1 m resolution true-color composite aerial photography data acquired in July–August 2014 by the U.S. Department of Agriculture National Agriculture Imagery Program.

7. Conclusions

The biomass burning science and data user community have for many years relied on coarser spatial resolution (≥1 km) satellite data to map and monitor fire-affected areas. Current operational satellite-based active fire detection systems provide routine observations of global fire activity, serving as input to a wide range of science applications, air quality monitoring, and strategic fire management. However, the lack of spatial fidelity typical of those satellite active fire products remains a major limitation preventing their application in landscape analyses and tactical fire management.

The ever-growing number of high and moderate spatial resolution earth observation systems, including Landsat-class instruments, is poised to change that reality. The launch in 2013 of Landsat-8 added

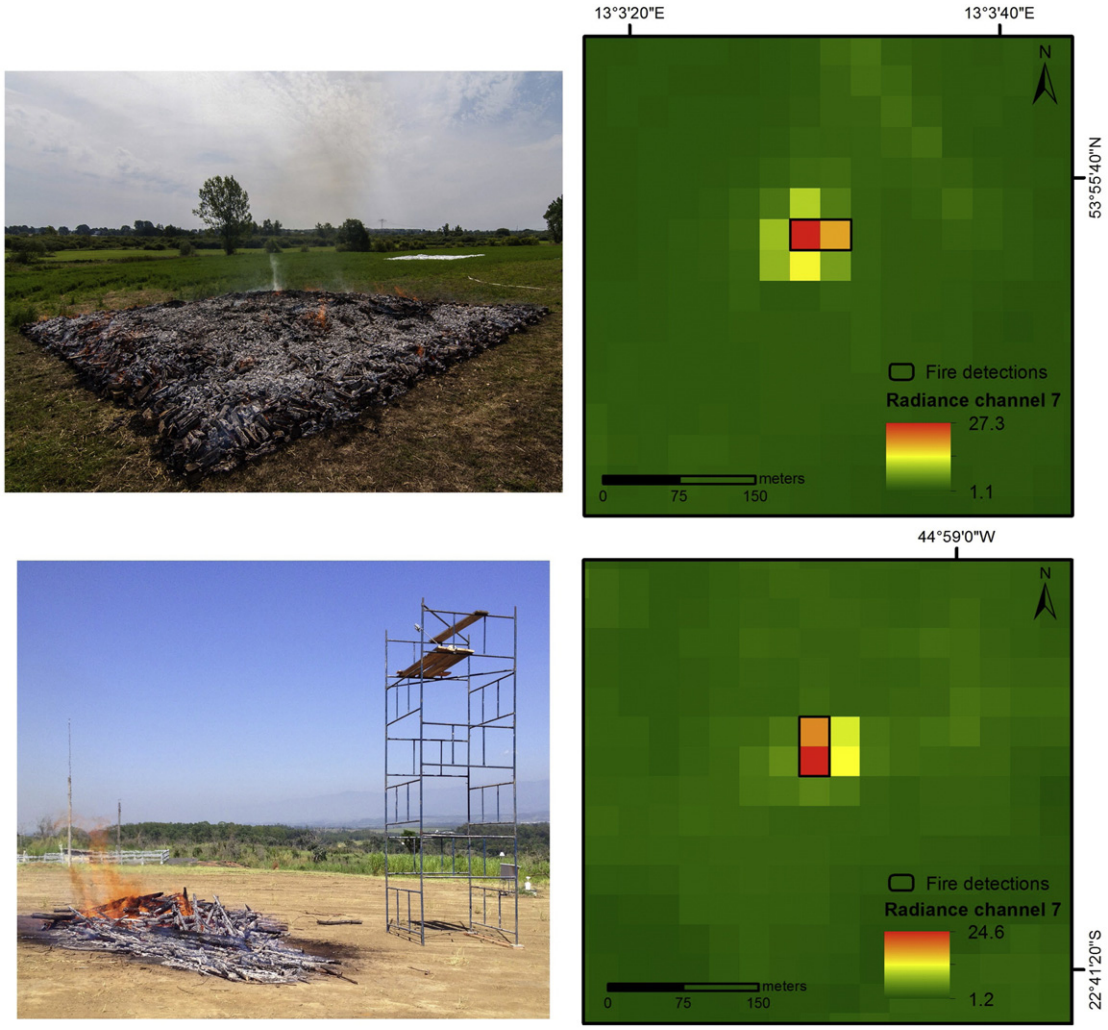

Fig. 7. Experimental fires used in support of Landsat-8 fire algorithm verification. The two rows show photos of the sites (left panels), and the OLI channel 7 image subset of the area with fire pixels marked in black (right panels). Top panels describe the 11×13 m^2 plot near Demmin/Germany (53.9276°N 13.0587°E) on 17 August 2013; bottom panels describe the 3×10 m^2 plot near Cachoeira Paulista/Brazil (22.6868°S 44.9844°W) on 19 January 2015.

to the existing network of science-quality moderate spatial resolution sensors; the ongoing planning and designing of the follow up Landsat-9 system could further extend the Landsat time series into the next decade. Most importantly, the comparatively recent shift towards an open data policy helped catapult the use of Landsat data among various science applications, including biomass burning. Complemented by other missions of similar scope (e.g., ESA/Sentinel-2), these emerging orbital systems have the potential to transform the way satellite data are used in support of fire science and management applications. Collectively, the integration of all available Landsat-class instruments in the near future could provide satellite-based spatially refined fire detection data at a temporal resolution frequent enough to support operational tactical fire management, adding to fire incident teams' limited array of spatially-explicit fire perimeter information.

Building on these new capabilities, we presented a new active fire algorithm using Landsat-8/OLI day and nighttime input data. The methodology expands on previous algorithms proposed for ASTER and Landsat-7/ETM+, incorporating additional visible and near-infrared channel data and a multi-temporal analysis scheme. Detailed analyses of the input OLI data indicated frequent saturation of fire-affected pixels on the fire-sensitive SWIR channel 7, and to a lesser extent of the NIR channel 6 data. Under more extreme conditions involving large or high intensity fires, channel 7 saturation was greatly exceeded resulting in radiometric artifacts associated with the folding of the pixel's digital number. In addition, visual inspection of the data corroborated by field verification indicated potential smearing of the fire-emitted radiance across adjacent pixels. We attributed the smearing effect to the resampling procedure involved in the production of the Level 1 T data files, and to residual stray light effects.

Despite those unique input data features, our assessment of the output fire classification data indicated good overall quality across a wide range of fire conditions observed in both day and nighttime imagery. Small and large-size biomass burning fires were successfully resolved, along with gas flares and active volcanoes. The high quality of the Level 1 T geolocation data provided improved co-location of pixels acquired on multiple dates enabling the post-processing of the fire algorithm output for persistent heat anomalies, and separation of potential false alarms. Overall commission errors were low, averaging 0.2% globally. Theoretical calculation of fire detection envelopes suggested significant improvement in performance compared to existing coarser spatial resolution fire products. Field verification data corroborated our theoretical assessment.

The spatially-refined active fire detection data provided by Landsat-class sensors create new opportunities and challenges for the user and science communities. Thanks to the improved fire line resolving capabilities, pixel-based analyses could be replaced by cluster-based application of the data where contiguous pixels are labeled accordingly and used to describe individual fire events. Such data application could

also lead to revised product assessment metrics describing omission and commission error rates based on clustering analyses. Detailed validation of these data remains a challenge as reference fire data sources are scarce and costly to acquire, currently demanding exhaustive image interpretation by expert image analysts. Future algorithm assessment should build on new complementary data sets (e.g., high resolution urban maps to identify potential false alarms over highly reflective buildings) and improved fire detection data simulation corroborated by field data acquired using new lower cost technologies (e.g., drones).

The increased availability of Landsat-class active fire data is fostering the development of new applications focused on landscape-scale analyses, including fire growth assessment, fire data assimilation into cutting-edge coupled weather-fire models, and tactical fire management, among others. In order to further maximize time-sensitive disaster monitoring applications, mission requirements should enable near real-time processing and distribution of the data. The global sampling strategy should also include comprehensive and systematic nighttime acquisitions of shortwave and thermal infrared data that can be used to more frequently track the progress of thermal anomalies.

The proposed algorithm was implemented at the USDA Remote Sensing Applications Center in Salt Lake City/UT, where it serves the U.S. fire management community. This and other Landsat-class active fire algorithms will continue to be developed and further refined. Future development of a fire disturbance essential climate variable will be pursued, complementing other satellite fire data sets in support of land-science applications.

Supplementary data to this article can be found online at http://dx.doi.org/10.1016/j.rse.2015.08.032.

Acknowledgments

We thank DLR, Erik Borg, and Doris Klein for hosting and sharing data from the small biomass burning experiment in Demmin/Germany on 17 August 2013. We also thank INPE for hosting the small biomass burning experiment on 19 January 2015 in Cachoeira Paulista/Brazil, and André Lima for sharing field data. Funding support for this study was provided by the NASA Applied Sciences Program (grant #NNX12AQ87G), the USDA Forest Service Remote Sensing Applications Center, and the GOES-R Algorithm Working Group at NOAA's National Environmental Satellite, Data, and Information Service. We thank four anonymous reviewers for their comments.

References

Anejionu, O. C. D., Blackburn, G. A., & Whyatt, J. D. (2014). Satellite survey of gas flares: Development and application of a Landsat-based technique in the Niger Delta. *International Journal of Remote Sensing, 35*(5), 1900–1925.

Asner, G. P., & Lobell, D. B. (2000). A biogeophysical approach for automated SWIR unmixing of soils and vegetation. *Remote Sensing of Environment, 74*, 99–112.

Bowman, D. M. J. S., Balch, J. K., Artaxo, P., Bond, W. J., Carlson, J. M., Cochrane, M. A., ... Pyne, S. J. (2009). Fire in the earth system. *Science, 324*, 481–484.

Casadio, S., Arino, O., & Serpe, D. (2012). Gas flaring monitoring from space using the ATSR instrument series. *Remote Sensing of Environment, 116*, 239–249.

Coen, J. L., & Schroeder, W. (2013). Use of spatially refined satellite remote sensing fire detection data to initialize and evaluate coupled weather-wildfire growth model simulations. *Geophysical Research Letters*. http://dx.doi.org/10.1002/2013GL057868.

Coen, J. L., & Schroeder, W. (2015). The high park fire: Coupled weather-wildland fire model simulation of a windstorm-driven wildfire in Colorado's front range. *Journal of Geophysical Research-Atmospheres, 120*. http://dx.doi.org/10.1002/2014JD021993.

Csiszar, I. A., & Schroeder, W. (2008). Short-term observations of the temporal development of active fires from consecutive same-day ETM+ and ASTER imagery in the Amazon: Implications for active fire product validation. *IEEE Journal of Selected Topics in Applied Earth Observations and Remote Sensing, 1*, 248–253.

Csiszar, I. A., Morisette, J. T., & Giglio, L. (2006). Validation of active fire detection from moderate-resolution satellite sensors: The MODIS example in Northern Eurasia. *IEEE Transactions on Geoscience and Remote Sensing, 44*(7), 1757–1764.

Csiszar, I., Schroeder, W., Giglio, L., Ellicott, E., Vadrevu, K., Justice, C. O., & Wind, B. (2014). Active fires from the Suomi NPP Visible Infrared Imaging Radiometer Suite: Product status and first evaluation results. *Journal of Geophysical Research-Atmospheres*, 119. http://dx.doi.org/10.1002/2013JD020453.

Davies, D. K., Ilavajhala, S., Wong, M. M., & Justice, C. O. (2009). Fire Information for Resource Management System: Archiving and distributing MODIS active fire data. *IEEE Transactions on Geoscience and Remote Sensing, 47*, 72–79.

Dwyer, J., Pinnock, S., Grégoire, J. -M., & Pereira, J. M. C. (2000). Global spatial and temporal distribution of vegetation fire as determined from satellite observations. *International Journal of Remote Sensing, 21*, 1289–1302.

Elvidge, C. D., Ziskin, D., Baugh, K. E., Tuttle, B. T., Ghosh, T., Pack, D. W., ... Zhizhin, M. (2009). A fifteen year record of global natural gas flaring derived from satellite data. *Energies, 2*, 595–622.

Elvidge, C. D., Zhizhin, M., Hsu, F. -C., & Baugh, K. E. (2013). VIIRS nightfire: Satellite pyrometry at night. *Remote Sensing, 5*, 4423–4449.

Flynn, L. P., Harris, A. J. L., & Wright, R. (2001). Improved identification of volcanic features using Landsat 7 ETM+. *Remote Sensing of Environment, 78*, 180–193.

Francis, P. W., & Rothery, D. A. (1987). Using the Landsat Thematic Mapper to detect and monitor active volcanoes: An example from Lascar volcano, northern Chile. *Geology, 15*, 614–617.

Freeman, J. P., Stohlgren, T. J., Hunter, M. E., Omi, P. N., Martinson, E. J., Chong, G. W., & Brown, C. S. (2007). Rapid assessment of postfire plant invasions in coniferous forests of the Western United States. *Ecological Applications, 17*, 1656–1665.

Giglio, L., Descloitres, J., Justice, C. O., & Kaufman, Y. J. (2003). An enhanced contextual fire detection algorithm for MODIS. *Remote Sensing of Environment, 87*, 273–282.

Giglio, L., Csiszar, I., & Justice, C. O. (2006). Global distribution and seasonality of fires as observed with the Terra and Aqua Moderate Resolution Imaging Spectroradiometer (MODIS) sensors. *Journal of Geophysical Research, 111*. http://dx.doi.org/10.1029/2005JG000142.

Giglio, L., Csiszar, I., Restás, Á., Morisete, J. T., Schroeder, W., Morton, D., & Justice, C. O. (2008). Active fire detection and characterization with the Advanced Spaceborne Thermal Emission and Reflection Radiometer (ASTER). *Remote Sensing of Environment, 112*, 3055–3063.

Giglio, L., Loboda, T. V., Roy, D. P., Quayle, B., & Justice, C. O. (2009). An active-fire based burned area mapping for the MODIS sensor. *Remote Sensing of Environment, 113*, 408–420.

Hantson, S., Padilla, M., Corti, D., & Chuvieco, E. (2013). Strengths and weaknesses of MODIS hotspots to characterize global fire occurrence. *Remote Sensing of Environment, 131*, 152–159.

Higgins, S. I., Bond, W. J., February, E. C., Bronn, A., Euston-Brown, D. I. W., Enslin, B., ... Trollope, W. S. W. (2007). Effects of four decades of fire manipulation on woody vegetation structure in savanna. *Ecological Applications, 88*, 1119–1125.

Ichoku, C., & Kaufman, Y. J. (2005). A method to derive smoke emission rates from MODIS fire radiative energy measurements. *IEEE Transactions on Geoscience and Remote Sensing, 43*, 2636–2649.

Ichoku, C., Giglio, L., Wooster, M. J., & Remer, L. A. (2008). Global characterization of biomass-burning patterns using satellite measurements of fire radiative energy. *Remote Sensing of Environment, 112*, 2950–2962.

Irons, J. R., Dwyer, J. L., & Barsi, J. A. (2012). the next landsat satellite: the landsat data continuity mission. *Remote Sensing of Environment, 112*, 11–21.

Kaiser, J. W., Heil, A., Andreae, M. O., Benedetti, A., Chubarova, N., Jones, L., ... van der Werf, G. (2012). Biomass burning emissions estimated with a global fire assimilation system based on observed fire radiative power. *Biogeosciences, 9*, 527–554.

Kasischke, E. S., Hewson, J. H., Stocks, B., van der Werf, G., & Randerson, J. (2003). The use of ATSR active fire counts for estimating relative patterns of biomass burning — A study from boreal forest region. *Geophysical Research Letters, 30*. http://dx.doi.org/10.1029/2003GL017859.

Kaufman, Y. J., Wald, A. E., Remer, L. A., Gao, B. -C., Li, R. -R., & Flynn, L. (1997). The MODIS 2.1 μm channel — Correlation with visible reflectance for use in remote sensing of aerosol. *IEEE Transactions on Geoscience and Remote Sensing, 35*, 1286–1298.

Larsen, I. J., MacDonald, L. H., Brown, E., Rough, D., Welsh, M. J., Pietraszek, J. H., ... Schaffrath, K. (2009). Causes of post-fire runoff and erosion: water repellency, cover or soil sealing? *Soil Science Society of America Journal, 73*, 1393–1407.

Liu, H., Randerson, J. T., Lindfors, J., & Chapin, F. S., III (2005). Changes in the surface energy budget after fire in boreal ecosystems of interior Alaska: An annual perspective. *Journal of Geophysical Research-Atmospheres*. http://dx.doi.org/10.1029/2004JD005158.

Loboda, T. V., & Csizar, I. (2007). Reconstruction of fire spread within wildland fire events in Northern Eurasia from the MODIS active fire product. *Global and Planetary Change, 56*, 257–273.

Loboda, T. V., O'Neal, K., & Csizar, I. (2007). Regionally adaptable dNBR-based algorithm for burned area mapping from MODIS data. *Remote Sensing of Environment, 109*, 429–442.

Mell, W. E., Manzello, S. L., Maranghides, A., Butry, D., & Rehm, R. G. (2010). The wildland-urban interface fire problem — Current approaches and research needs. *International Journal of Wildland Fire, 19*, 238–351.

Morfitt, R., Barsi, J., Levy, R., Markham, B., Micijevic, E., Ong, L., ... Vanderwerff, K. (2015). Landsat-8 Operational Land Imager (OLI) radiometric performance on-orbit. *Remote Sensing, 7*, 2208–2237.

Morisette, J. T., Giglio, L., Csiszar, I., & Justice, C. O. (2005). Validation of the MODIS active fire product over Southern Africa with ASTER data. *International Journal of Remote Sensing, 26*(19), 4239–4264.

Oliva, P., & Schroeder, W. (2015). Assessment of VIIRS 375 m active fire detection product for direct burned area mapping. *Remote Sensing of Environment, 160*, 144–155.

Oliveras, I., Meirelles, S. T., Hirakuri, V. L., Freitas, C. R., Miranda, H. S., & Pivello, V. R. (2012). Effects of fire regimes on herbaceous biomass and nutrient dynamics in the Brazilia savanna. *International Journal of Wildland Fire, 22*, 368–380.

Oppenheimer, C. (1991). Lava flow cooling estimated from Landsat Thematic Mapper data: The Lonquimay Eruption (Chile, 1989). *Journal of Geophysical Research, 96*. http://dx.doi.org/10.1029/91JB01902.

Pozo, D., Olmo, F. J., & Alados-Arboledas, L. (1997). Fire detection and growth monitoring using a multitemporal technique on AVHRR mid-infrared and thermal channels. *Remote Sensing of Environment*, *60*, 111–120.

Roy, D., Wulder, M. A., Loveland, T. R., Woodcock, C. E., Allen, R. G., Anderson, M. C., ... Zhu, Z. (2014). Landsat-8: Science and product vision for terrestrial global change research. *Remote Sensing of Environment*, *145*, 154–172.

Schoennagel, T., Nelson, C. R., Theobald, D. M., Carnwath, G. C., & Chapman, T. B. (2009). Implementation of National Fire Plan treatments near the wildland-urban interface in the western United States. *Proceedings of the National Academy of Sciences*, *106*, 10706–10711.

Schroeder, W., Prins, E., Giglio, L., Csiszar, I., Schmidt, C., Morisette, J., & Morton, D. (2008a). Validation of GOES and MODIS active fire detection products using ASTER and ETM + data. *Remote Sensing of Environment*, *112*, 2711–2726.

Schroeder, W., Ruminski, M., Csiszar, I., Giglio, L., Prins, E., Schmidt, C., & Morisette, J. (2008b). Validation analyses of an operational fire monitoring product: The hazard mapping system. *International Journal of Remote Sensing*, *29*, 6059–6066.

Schroeder, W., Oliva, P., Giglio, L., & Csiszar, I. (2014). The new VIIRS 375 m active fire detection data product: Algorithm description and initial assessment. *Remote Sensing of Environment*, *143*, 85–96.

U.S. Department of the Interior – U.S. Geological Survey (2013). LDCM CAL/VAL Algorithm Description Document, version 3.0. Digital document available at: http://landsat.usgs.gov/documents/LDCM_CVT_ADD.pdf (last accessed 22 June 2015)

Van der Werf, G. R., Randerson, J. T., Giglio, L., Collatz, G. J., Mu, M., Kasibhatla, P. S., ... van Leeuwen, T. T. (2010). Global fire emissions and the contribution of deforestation, savanna, forest, agricultural, and peat fires (1997–2009). *Atmospheric Chemistry and Physics*, *10*, 11707–11735.

Vermote, E., Ellicott, E., Dubovik, O., Lapyonok, T., Chin, M., Giglio, L., & Roberts, G. J. (2009). An approach to estimate global biomass burning emissions of organic and black carbon from MODIS fire radiative power. *Journal of Geophysical Research*, *114*. http://dx.doi.org/10.1029/2008JD011188.

Wiedinmyer, C., Quayle, B., Geron, C., Belote, A., McKenzie, D., Zhang, X., ... Wynne, K. K. (2006). Estimating emissions from fires in North America for air quality modeling. *Atmospheric Environment*, *40*, 3419–3432.